Earth and Planetary Science Letters 403 (2014) 418–431

Contents lists available at ScienceDirect

Earth and Planetary Science Letters

www.elsevier.com/locate/epsl

# Developing an inverted Barrovian sequence; insights from monazite petrochronology

Catherine M. Mottram [a,b,*], Clare J. Warren [a], Daniele Regis [a,c], Nick M.W. Roberts [d], Nigel B.W. Harris [a], Tom W. Argles [a], Randall R. Parrish [d,e]

[a] Department of Environment, Earth and Ecosystems, Centre for Earth, Planetary, Space and Astronomical Research (CEPSAR), The Open University, Walton Hall, Milton Keynes, MK7 6AA, UK
[b] Department of Earth Science, University of California, Santa Barbara, CA 93106, USA
[c] Department of Geology and Geophysics, University of Calgary, Calgary, Alberta, T2N 1N4, Canada
[d] NERC Isotope Geosciences Laboratory, British Geological Survey, Keyworth, Nottingham NG12 5GG, UK
[e] Department of Geology, University of Leicester, University Road, Leicester, LE1 7RH, UK

ARTICLE INFO

*Article history:*
Received 20 March 2014
Received in revised form 6 July 2014
Accepted 8 July 2014
Available online 7 August 2014
Editor: T.M. Harrison

*Keywords:*
inverted metamorphism
ductile thrusting
petrochronology
monazite geochronology

ABSTRACT

In the Himalayan region of Sikkim, the well-developed inverted metamorphic sequence of the Main Central Thrust (MCT) zone is folded, thus exposing several transects through the structure that reached similar metamorphic grades at different times. *In-situ* LA-ICP-MS U–Th–Pb monazite ages, linked to pressure–temperature conditions *via* trace-element reaction fingerprints, allow key aspects of the evolution of the thrust zone to be understood for the first time. The ages show that peak metamorphic conditions were reached earliest in the structurally highest part of the inverted metamorphic sequence, in the Greater Himalayan Sequence (GHS) in the hanging wall of the MCT. Monazite in this unit grew over a prolonged period between ~37 and 16 Ma in the southerly leading-edge of the thrust zone and between ~37 and 14.5 Ma in the northern rear-edge of the thrust zone, at peak metamorphic conditions of ~790 °C and 10 kbar. Monazite ages in Lesser Himalayan Sequence (LHS) footwall rocks show that identical metamorphic conditions were reached ~4–6 Ma apart along the ~60 km separating samples along the MCT transport direction. Upper LHS footwall rocks reached peak metamorphic conditions of ~655 °C and 9 kbar between ~21 and 16 Ma in the more southerly-exposed transect and ~14.5–12 Ma in the northern transect. Similarly, lower LHS footwall rocks reached peak metamorphic conditions of ~580 °C and 8.5 kbar at ~16 Ma in the south, and 9–10 Ma in the north. In the southern transect, the timing of partial melting in the GHS hanging wall (~23–19.5 Ma) overlaps with the timing of prograde metamorphism (~21 Ma) in the LHS footwall, confirming that the hanging wall may have provided the heat necessary for the metamorphism of the footwall.

Overall, the data provide robust evidence for progressively downwards-penetrating deformation and accretion of original LHS footwall material to the GHS hanging wall over a period of ~5 Ma. These processes appear to have occurred several times during the prolonged ductile evolution of the thrust. The preserved inverted metamorphic sequence therefore documents the formation of sequential 'paleo-thrusts' through time, cutting down from the original locus of MCT movement at the LHS–GHS protolith boundary and forming at successively lower pressure and temperature conditions. The petrochronologic methods applied here constrain a complex temporal and thermal deformation history, and demonstrate that inverted metamorphic sequences can preserve a rich record of the duration of progressive ductile thrusting.



## 1. Introduction

Inverted metamorphic sequences are commonly associated with fault zones, such as in the soles of ophiolites (Jamieson, 1986; Kidder et al., 2013), and in continental collisional thrusts zones, such as in the Caledonides (Andreasson and Lagerblad, 1980), the Appalachians (Camiré et al., 1995), the Variscan belt (Burg et al., 1984; Pitra et al., 2010), the Canadian Cordillera (Crowley and Parrish, 1999; Gibson et al., 1999) and the Himalaya (Gansser, 1964). In these locations, an apparent inverted metamorphic field gradient is preserved, whereby the pressure–temperature ($P$–$T$) conditions of rock formation decrease with structural depth. As inverted

* Corresponding author at: Department of Environment, Earth and Ecosystems, Centre for Earth, Planetary, Space and Astronomical Research (CEPSAR), The Open University, Walton Hall, Milton Keynes, MK7 6AA, UK.
*E-mail address:* catherine.mottram@open.ac.uk (C.M. Mottram).

http://dx.doi.org/10.1016/j.epsl.2014.07.006

metamorphic sequences are intimately related to major mountain-building structures, they preserve a record of ductile thrusting processes. These zones therefore provide an ideal natural laboratory to explore the thermal and temporal evolution of a fundamental geological mechanism in continental collisional events.

In the Himalayan orogen, the duration and conditions of thrusting have been traditionally addressed using a combination of thermobarometric and geochronological data, through the use of monazite geochronology, pseudosection modelling, and less commonly, major and accessory phase geochemical analysis (e.g. Bollinger and Janots, 2006; Catlos et al., 2001; Crowley and Parrish, 1999; Gibson et al., 1999; Goscombe and Hand, 2000; Groppo et al., 2009; Kohn et al., 2001; Stephenson et al., 2000; Vannay and Grasemann, 2001; Yakymchuk and Godin, 2012). Monazite analysis frequently yields complex geochronological datasets (e.g. Buick et al., 2006; Gasser et al., 2012; Hermann and Rubatto, 2003), making it difficult to link the ages with the $P$–$T$ conditions and crystallisation reactions of the phases. Emerging developments in linking 'age to stage', and particularly the use of combined petrography and trace-element data from major and accessory phases (petrochronology), allow high-spatial precision geochronological data to be more firmly linked to the $P$–$T$ conditions of accessory phase crystallisation reactions (Foster et al., 2004; Gasser et al., 2012; Janots et al., 2008; Rubatto et al., 2013). This is achieved by detailed observation of textural relationships, geochemical analysis of coexisting accessory phases and systematic documentation of trace-element signatures in major phases that 'fingerprint' monazite-forming reactions (Foster et al., 2002, 2000, 2004; Gasser et al., 2012; Hermann and Rubatto, 2003; Hoisch et al., 2008; Janots et al., 2006, 2007, 2008, 2009; Kingsbury et al., 1993; Pyle and Spear, 2003; Rubatto et al., 2006; Smith and Barreiro, 1990; Spear, 2010; Wing et al., 2003). Such advances in metamorphic and geochronological analysis offer the potential to unravel the complex tectonic and thermal evolution of thrust zones associated with inverted metamorphism.

This study presents a comprehensive, 4D (pressure–temperature–time–deformation) examination of the inverted Barrovian metamorphic sequence beneath the Himalayan Main Central Thrust in the Sikkim region of India. Petrochronology techniques that combine petrography, thermobarometric calculations, geochronological data, and trace-element geochemistry link the timing of prograde, peak and retrograde metamorphic conditions across three structural transects. Our data show that (1) the timing of peak metamorphism decreases structurally downwards from the initial thrust surface into the lower grade metamorphic rocks; (2) the timing of attainment of the same grade of peak metamorphism varies by ca. 4–6 Ma around the exposed MCT rocks in the Sikkim Himalaya and (3) the timing of melting in the hanging wall was, in some instances, contemporaneous with prograde or peak metamorphism in the proximal footwall. Overall, our data show that the MCT in Sikkim was active for at least 11 Ma during the Miocene.

## 2. Geological setting

The Himalayan orogen exposes one of the Earth's largest and best-preserved inverted Barrovian metamorphic sequences, which developed during thrusting along the 2500 km-long Main Central Thrust (MCT: Fig. 1; Catlos et al., 2001; Goscombe and Hand, 2000; Groppo et al., 2010; Kohn et al., 2001; Paudel and Arita, 2000; Sinha-Roy, 1982; Stephenson et al., 2000; Vannay and Grasemann, 2001; Vannay et al., 1999; Yakymchuk and Godin, 2012). The Darjeeling hills and Sikkim (collectively known as the Sikkim Himalaya) in the eastern Himalaya, represent the ideal location for studying the MCT (Fig. 1). During the Eocene-Recent collision of India and Asia, Indian crustal rocks were buried to crustal depths of

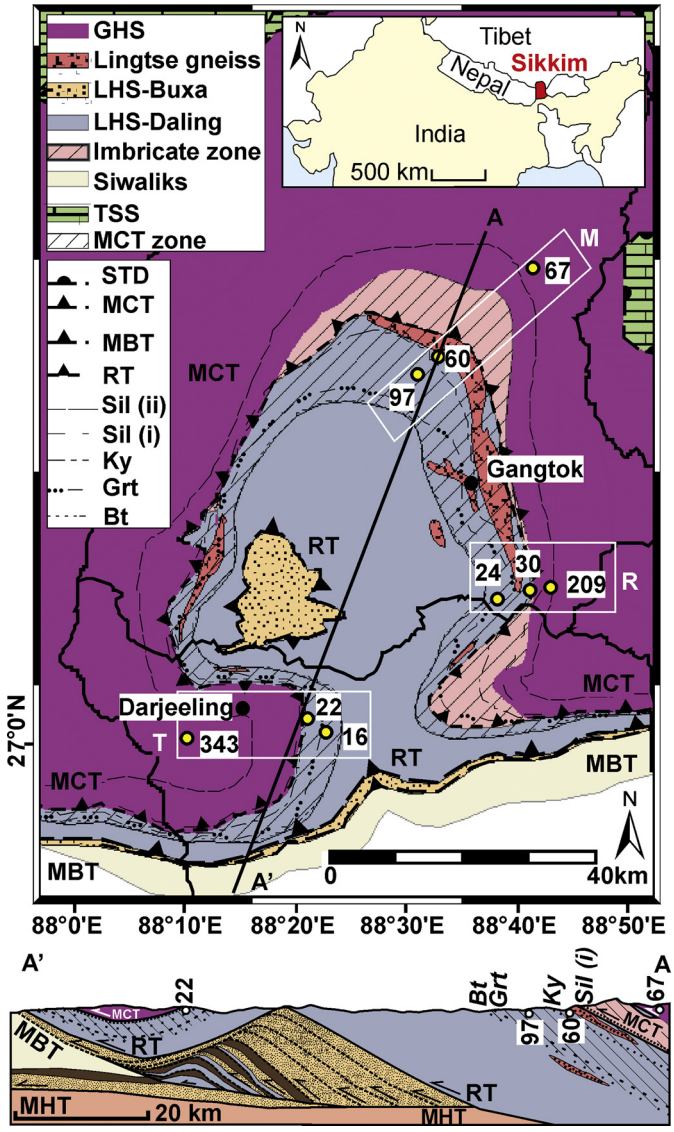


**Fig. 1.** Geological map and cross section (to scale) of the Sikkim Himalaya, adapted from Mottram et al. (2014). Sample locations are shown for the three boxed transects (T = Takdah, M = Mangan and R = Rongli). Abbreviations: STD = South Tibetan Detachment, MCT = Main Central Thrust, RT = Ramgarh Thrust, MBT = Main Boundary Thrust, MHT = Main Himalayan Thrust, Sil (ii) = sillimanite (no muscovite), Sil (i) = fibrolite, Ky = kyanite, Grt = garnet, Bt = biotite. GHS = Greater Himalayan Sequence, LHS = Lesser Himalayan Sequence, B = Buxa, D = Daling, IZ = Imbricate Zone (Mottram et al., 2014), SW = Siwaliks, TSS = Tethyan Sedimentary Sequence. Lesser Himalayan Duplex schematic representation of Bhattacharyya and Mitra (2009). The zone of deformation associated with the Main Central Thrust is shown as a hatched area.

20–30 km before being exhumed by a combination of tectonic and surface processes. Miocene-aged movement along the MCT juxtaposed two isotopically distinct rock packages, the Greater and Lesser Himalayan Sequences, which originally formed the proximal and distal parts of the Indian margin (Mottram et al., 2014 and references therein). The MCT therefore represents both a protolith boundary and a wide zone of ductile shear. The ~10 km thick thrust zone was folded after motion along it ceased, by an underlying late-stage duplex. This dome provides exposures of several different structural levels and 'time-windows' through the MCT zone (Bhattacharyya and Mitra, 2009; Fig. 1).

The inverted Barrovian zone consists of a ca. 10 km (map view) wide package of pelitic schists characterised by a well-developed penetrative schistosity, mineral stretching lineations that lie parallel to the southerly thrusting direction, and well-preserved assem-

blages of Barrovian-sequence index minerals (Fig. 1 and supplementary material S2.1–2.3; Mohan et al., 1989). Peak metamorphic conditions increase structurally upwards from ~480 to 530 °C and 5 kbar in the structurally low garnet zone, through ~540–565 °C and 6 kbar in the staurolite zone, ~565–625 °C and 6–7 kbar in the kyanite zone, ~675 °C and 7.5 kbar in the sillimanite zone and ~625–700 °C and 6–9 kbar in the uppermost sillimanite–K-feldspar zone (Dasgupta et al., 2009, 2004; Dubey et al., 2005).

Samples of GHS, upper LHS and lower LHS material were collected from three transects across the deformed MCT 'zone': Takdah in the south-west, Mangan in the north and Rongli in the east (Fig. 1).

## 3. Methods

### 3.1. Electron Probe Micro-Analysis (EPMA) and scanning electron microscope (SEM)

Major elements in all minerals were analysed in polished thin section using the Open University Cameca SX100 EPMA. Mineral formulae were calculated on the basis of 12 oxygen for garnet, 8 for feldspars, 22 for micas and 46 for staurolite. Elemental X-ray maps of monazite, garnet and whole thin sections were produced using the EPMA and the Open University FEI Quanta 3D dual beam microscope SEM. Full operating conditions can be found in the supplementary material S.1.1–1.2.

### 3.2. Pressure–temperature calculations and modelling

Estimates of peak $P$–$T$ were calculated using the Ti-in-biotite calculation of Henry et al. (2005), the garnet-biotite thermometer of Bhattacharya et al. (1992), the garnet–$Al_2SiO_5$–plagioclase (GASP) barometer of Powell and Holland (1988) and the Zr-in-rutile calibration of Tomkins et al. (2007), calculated at 9 kbar pressure.

Pseudosections of samples 16, 22, 60, 67 and 343 were constructed using Perple_X_6.6.8 (Connolly 1990, 2009) using the internally consistent thermodynamic dataset and equation of state for $H_2O$ of Holland and Powell (2011). Samples were modelled in the system MnNKCFMASTH. $Fe^{3+}$ was ignored because there were no $Fe^{3+}$-rich oxides in the assemblages and the allocated $Fe^{3+}$ in analysed phases was negligible. The addition of $Fe^{3+}$ to the bulk composition did not affect the overall topology of the final pseudosections (supplementary material S3.4). Pseudosections were calculated under fluid-saturated ($aH_2O = 1$) conditions for samples that equilibrated under subsolidus conditions, and with $H_2O$ as a component for suprasolidus samples. The $H_2O$ content was calculated from the modal proportion of biotite, using the Ti–H substitution scheme of White et al. (2007). The bulk composition of each sample was calculated to represent the effective composition of the equilibrium volume either from an adapted XRF composition of the rock, or from calculating of the proportion of each mineral phase in the sample from analysis of thin section X-ray maps using ImageJ analysis software (supplementary material S3.4; Schneider et al., 2012).

The $P$–$T$ conditions were constrained by comparing calculated weight% oxide isopleths of garnet (CaO, FeO and MgO) and plagioclase (CaO, $Na_2O$) with observed compositions of those phases where present. As garnet zoning has a significant fractionation effect on the local effective bulk composition, it was necessary to consider two different effective bulk compositions in samples that showed significant garnet zoning, in order to calculate the conditions of garnet core and rim growth (Evans, 2004; Gaidies et al., 2006). The construction of garnet isopleths then allowed for the comparison of the corresponding garnet core or rim compositions. Full methods and solution models used are documented in the supplementary material S1.3.

### 3.3. U–Th–Pb monazite geochronology

U–Th–Pb concentrations in monazite were analysed at the NERC Isotope Geosciences Laboratories (NIGL), UK, using a Nu Attom sector-field single-collector inductively coupled plasma mass spectrometer (SC-ICP-MS) and New Wave Research UP193ss (193 nm) Nd:YAG laser ablation system. Monazites were commonly zoned in Y and Th, which were used to select suitable analysis points using laser conditions of 15 μm spot size at 5 Hz and ~2.5 $J\,cm^{-2}$ fluence (supplementary material S4.2).

The instrumental configuration and measurement procedures follow previous methods (Palin et al., 2013), and full analytical conditions are shown in the supplementary material S1.4. The monazite 'Stern' was used as the primary reference and 'Manangotry' and 'Moacyr' were used as secondary reference materials (Palin et al., 2013). Overall reproducibility achieved on the secondary reference material was <3% (2 SD) for U–Pb ages.

All data were processed using an in-house spreadsheet calculation routine. Full data tables of data can be found in the supplementary data tables. A $^{207}Pb$-based common lead correction was applied to the U–Pb and Th–Pb ages. A further correction was made to the common lead corrected ages to account for excess $^{206}Pb$ derived from $^{230}Th$, an intermediate daughter nuclide in the $^{238}U$ decay series. Uncorrected monazite data were plotted on Tera–Wasserburg plots, using Isoplot 4.14 (Ludwig, 2003), with intercept ages extrapolated from a $^{207}Pb/^{206}Pb$ ratio of $0.83 \pm 0.02$ (Stacey and Kramers, 1975). For samples with a sparse distribution of monazite spot ages, an MSWD is not quoted as it was not possible to constrict an intercept age through the array.

Both U–Pb and Th–Pb decay schemes can be used to date monazites (common-Pb ages shown in full data tables). Excess $^{206}Pb$ incorporated into monazite during crystallisation can cause the $^{238}U/^{206}Pb$ ages to appear older than the true crystallisation age, which is thought to be particularly significant in Cenozoic monazites. The common-Pb-corrected $^{232}Th/^{208}Pb$ ages have therefore been regarded as more accurate (Parrish, 1990). However in this study, due to the acquisition protocol, the $^{232}Th/^{208}Pb$ ages are typically less precise than the $^{238}U/^{206}Pb$ ages. We therefore quote the $^{238}U/^{206}Pb$ ages and uncertainties ($\pm 2\sigma$) when referring to the age of monazite populations.

### 3.4. Trace-element data

Monazite and garnet trace-element and Zr-in-rutile concentrations were acquired on the Open University Agilent 7500 quadrupole ICP-MS coupled to a New Wave Research UP213 (213 nm) Nd:YAG laser ablation system. The same monazites selected for U–Th–Pb dating were analysed *in-situ* in polished thin sections for REE concentrations. Laser spots for REE-analysis were sited either immediately next to, or as a larger spot engulfing, the pits formed during the U–Th–Pb analyses (see supplementary material S4.2.10 for images of pits). NIST-610 and 612 synthetic glasses were used as primary and secondary standards. Internal standardisation was to CeO for monazite and CaO for garnet using values measured by EPMA. Garnet analyses were screened for accessory phase interference (e.g. Zr for zircon and P for monazite). REE concentrations were normalised to chondritic values of McDonough and Sun (1995). Full data tables, running conditions and reproducibility of standards are documented in supplementary material S1.5.

## 4. Results

### 4.1. Petrology and mineral chemistry

The structurally highest samples (343, from the Takdah section, 67, from the Mangan section, and 209, from the Rongli section), are Greater Himalayan $Al_2SiO_5$-bearing gneisses/migmatites.

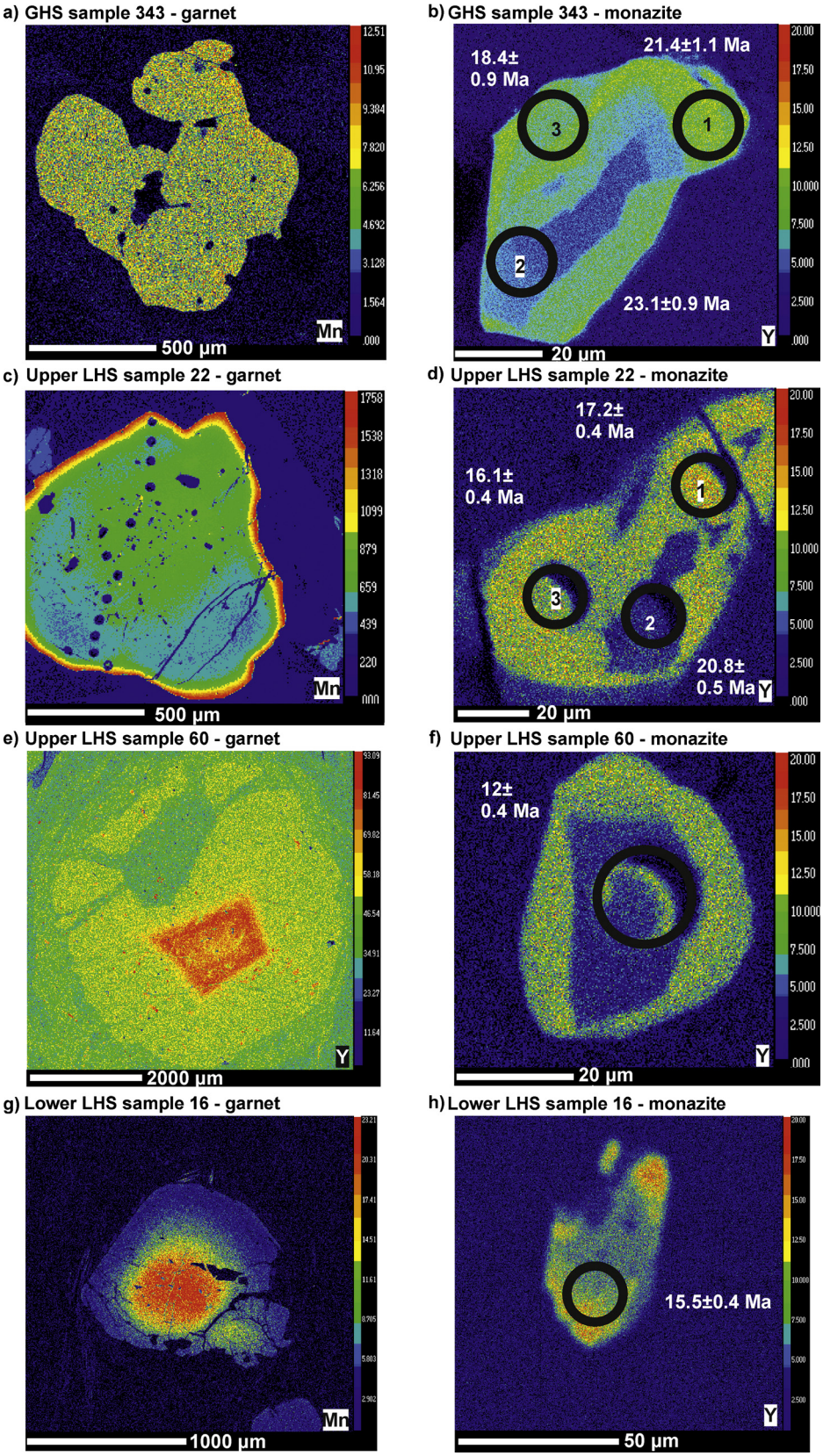


**Fig. 2.** Garnet (a, c, e, g) and monazite (b, d, f, h) X-ray maps demonstrating zoning in major (Mn) and trace (Y) elements. Monazite maps show $^{238}U/^{206}Pb$ ages with $2\sigma$ errors.

Sample 343 is described in detail here; other samples reached similar peak conditions and are described in supplementary material S2. Sample 343 contains garnet + kyanite + sillimanite + biotite + plagioclase + K-feldspar + quartz + rutile + apatite + monazite + xenotime + zircon. Garnets are unzoned in major elements (Fig. 2a), contain inclusions of monazite and yield an

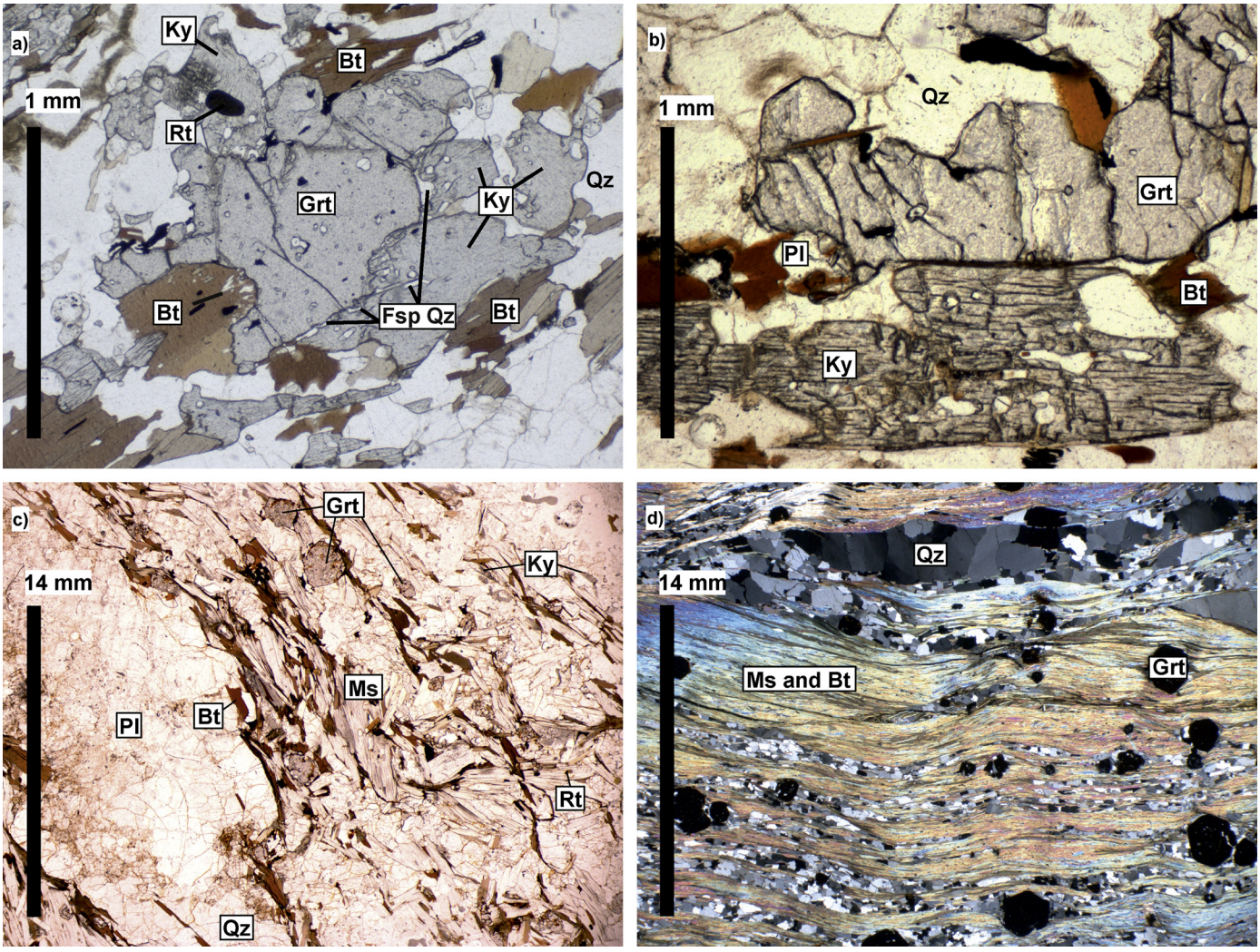


**Fig. 3.** Photomicrographs of samples from the Takdah transect. (A) Sample 343, garnet kyanite migmatite. This image shows intergrown garnet and kyanite grains, feldspar-biotite products of a back-reaction with melt and garnet, and thin layers of feldspar and quartz around and between the garnet and kyanite (plane polarised light). (B) Sample 343 quartz embayments and lobate inclusions in garnet and kyanite (plane polarised light). (C) Sample 22, coarse-grained garnet–kyanite–staurolite schist, shown in plane polarised light. (D) Sample 16, garnet–staurolite pelitic schist shown in cross polarised light. Bt = biotite, Fsp = feldspar, Grt = garnet, Ky = kyanite, Ms = muscovite, Pl = plagioclase, Qz = quartz, Rt = rutile.

average composition of $X_{Ca} = 0.04$, $X_{Mg} = 0.17$, $X_{Fe} = 0.76$ and $X_{Mn} = 0.03$ (full EPMA results are documented in supplementary material S2.4). Kyanite and garnet are interpreted to be peritectic phases, displaying textures such as irregular, bulbous and lobate quartz inclusions and embayments and surrounding thin films of feldspar and quartz (Fig. 3a–b + supplementary material S3.3). The biotite, plagioclase and sillimanite that commonly surround garnet are interpreted as the localised products of a back-reaction between melt and garnet (Fig. 3a). The main population of biotite has a composition of $X_{Mg} = 0.43$ and displays 'lath-shaped' domains of intergrown biotite and quartz (supplementary material S2.3). These features are all indicative that these phases coexisted with melt (Groppo et al., 2010; Waters, 2001).

The upper LHS samples (22, Takdah; 60, Mangan; and 30, Rongli), located near the GHS–LHS protolith boundary (Mottram et al., 2014), are kyanite-bearing schists. Sample 22 is described in detail; the other samples reached similar peak conditions and are described in supplementary material S2. Sample 22 is a coarse-grained kyanite schist containing garnet + staurolite + kyanite + biotite + muscovite + plagioclase + quartz + sillimanite + ilmenite + tourmaline + rutile + apatite + monazite + xenotime + zircon. Kyanite and staurolite are texturally in equilibrium, with neither phase displaying breakdown textures. The sample contains muscovite grains up to 10 mm across, which form a weak schistosity (Fig. 3c). Garnets contain inclusions of allanite, monazite, xenotime, zircon, ilmenite and rutile and are unzoned in major elements, except for Mn which shows normal diffusion zoning at rims (Fig. 2c), with an average composition of $X_{Ca} = 0.05$, $X_{Mg} = 0.15$, $X_{Fe} = 0.73$ and $X_{Mn} = 0.06$. Biotite has a composition of $X_{Mg} = 0.45$.

The structurally lowest LHS samples (16, Takdah; 97, Mangan; and 24, Rongli) are (garnet-staurolite) mica schists. Sample 16 is described in detail but the other samples reached similar peak conditions and are described in detail in supplementary material S2. Sample 16 is a garnet-staurolite schist containing garnet + staurolite + biotite + muscovite + quartz + ilmenite + monazite + apatite + allanite + zircon. The sample has a well-developed schistosity forming an undulating fabric, with deformed quartz lenses (Fig. 3d). Garnets contain syn-kinematic inclusion trails of allanite, monazite and ilmenite, and are zoned in major elements (Fig. 2g) with core compositions of $X_{Ca} = 0.06$, $X_{Mg} = 0.09$, $X_{Fe} = 0.78$ and $X_{Mn} = 0.07$ and rim compositions of $X_{Ca} = 0.02$, $X_{Mg} = 0.11$, $X_{Fe} = 0.85$ and $X_{Mn} = 0.02$. Biotite has an $X_{Mg}$ value of 0.44. The main mica-rich foliation wraps the garnets, and pressure shadows are well-developed.

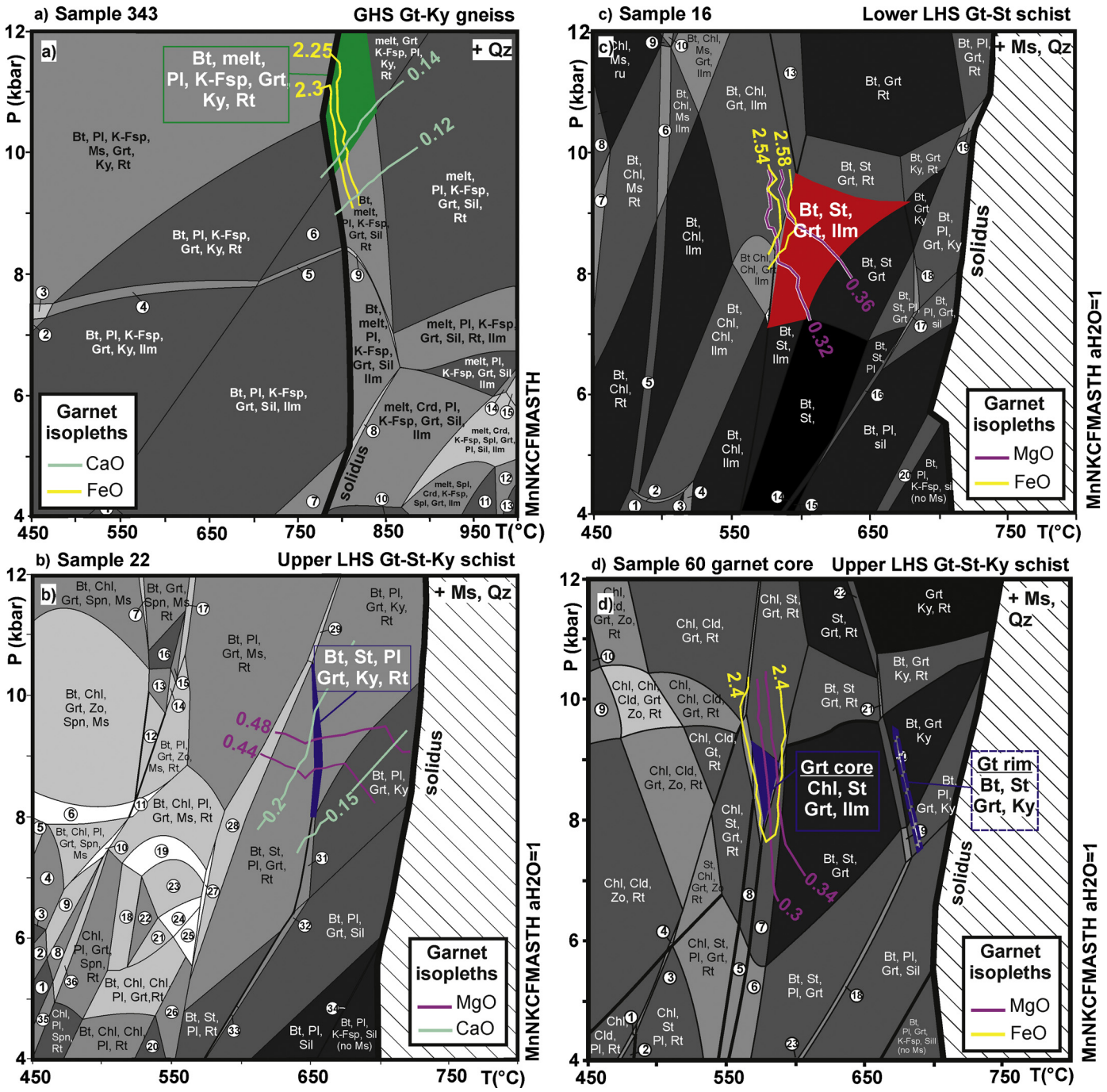


**Fig. 4.** Pseudosections for samples 16, 22, 343, from the Takdah transect and sample 60 from the Mangan section. The peak field is shaded for each pseudosection. Compositional garnet isopleths constrain the peak assemblage, additional isopleths are shown in the supplementary material S3.4. Samples which equilibrated under subsolidus conditions (16, 22 and 60) are modelled in the system MnNKCFMASTH under $H_2O$-saturated conditions. The area above the solidus for these samples was not modelled (hatched area). Sample 343 which equilibrated above the solidus is modelled with $H_2O$ as a component in the MnNKCFMASTH system. Phases in saturation are shown in the top right of each diagram. Full pseudosections with numbered fields are shown in the supplementary material S3.4. (A) Pseudosection for sample 343, peak field is shaded in green (biotite, melt, plagioclase, K-feldspar, garnet, kyanite and rutile at 790 °C and 10 kbar). (B) Pseudosection for sample 22 has a peak field shaded in blue (biotite, staurolite, plagioclase, garnet, kyanite and rutile) at 655 °C and 9 kbar. (C) Pseudosection for sample 16, peak field is shown in red (biotite, staurolite, garnet and ilmenite) at ~580 °C and 8.5 kbar. (D) Pseudosection for sample 60, drawn for a bulk composition representing the garnet core assemblage, this prograde assemblage is shaded in blue (chlorite, staurolite, garnet and ilmenite) at ~550 °C and 9 kbar. The peak metamorphic assemblage for this sample was calculated in a separate pseudosection (supplementary material S3.4.4.4) with the bulk composition for the garnet rim and is shown as the dashed blue field (biotite, staurolite, garnet and kyanite). This is equivalent to the same field for sample 22 and supports the suggestion that the upper LHS samples had a similar prograde and peak metamorphic history. (For interpretation of the references to colour in this figure legend, the reader is referred to the web version of this article.)

### 4.2. *P–T* evolution

Calculated pseudosections are shown in detail in Fig. 4 and summarised in Fig. 5. Further detail is provided in supplementary material S3.4. The pseudosection results are supported by average *P–T*, Ti-in-biotite and Zr-in-rutile calculations (Fig. 5, and supplementary data S3.1–3.3), which demonstrate that samples collected from the same structural levels in the three transects experienced similar *P–T* conditions.

The GHS rocks equilibrated at peak conditions around the kyanite–sillimanite transition in the presence of melt. This is shown in the pseudosection of sample 343, which shows that the

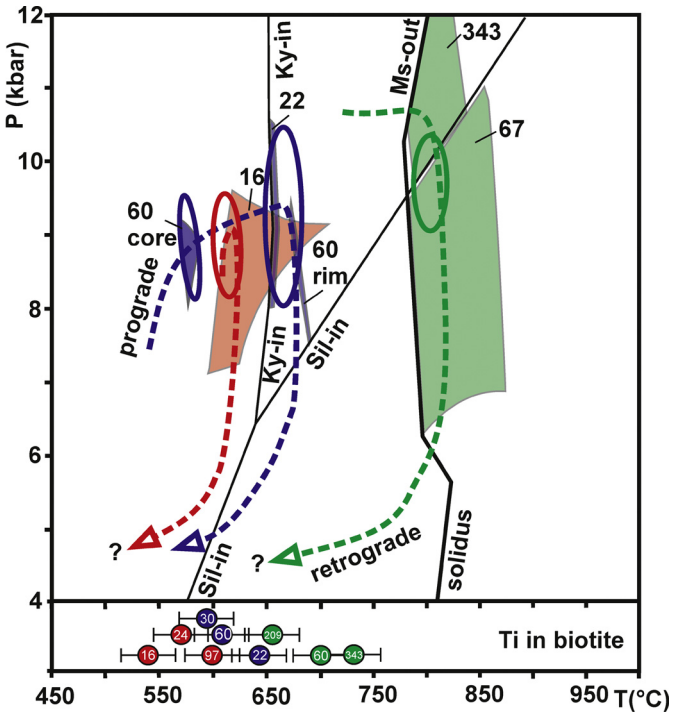


**Fig. 5.** Summary of pressure–temperature conditions for all samples. The lowest grade LHS samples are represented by the red field and arrow (sample 16 and representative of samples 24 and 97). The upper LHS samples have a more prolonged prograde and peak history as demonstrated by the blue fields and arrow for samples 22 and 60 (representative of sample 30). The peak metamorphic fields for the GHS samples are shown in green and by the green arrow (for samples 67 and 343 and representative of sample 209). Ti in biotite measurements are shown in the lower box. As the thermometer is calibrated for pressures of ~4–6 kbar (Henry et al., 2005), somewhat lower than the ambient pressure conditions, a conservative error of ±50 °C has been applied to each measurement. (For interpretation of the references to colour in this figure legend, the reader is referred to the web version of this article.)

peak assemblage of biotite, garnet, K-feldspar, kyanite, melt, plagioclase and rutile was stable at ~790 °C and ~ 10 kbar, above the solidus (Fig. 4). Sample 67, from the Mangan section, equilibrated at similar conditions (~800 °C and ~9.5 kbar) represented by the stability field of biotite, melt, garnet, plagioclase, K-feldspar, sillimanite and quartz (supplementary material S3.4.4.2). The presence of spinel (hercynite composition) in a garnet gneiss collected at the same locality as 67 and comparable in lithology (sample 72 in supplementary data S2), suggests that the rocks decompressed isothermally to relatively low pressures, where spinel formed (Baldwin et al., 2007).

The prograde history of the upper LHS rocks is calculated from sample 60, in which garnet preserves significant prograde growth zoning (Fig. 2e). The pseudosection calculated for the garnet core composition (Fig. 4), demonstrates that garnet equilibrated at conditions of ~550 °C and ~9 kbar. The garnet rim grew in association with biotite, staurolite, kyanite, garnet, quartz and white mica at ~675 °C and ~9 kbar (supplementary material S3.4.4.4). Sample 22, with the peak assemblage biotite, staurolite, plagioclase, garnet, kyanite and rutile, equilibrated at similar conditions of ~655 °C and ~9 kbar (Fig. 4). The peak estimates are supported by Zr-in-rutile thermometer calculations, which yield temperatures of 675 ± 9 °C (supplementary material S3.3). The retrograde history of the upper LHS rocks is constrained by the appearance of fibrolite needles in samples 22 and 30, evidence that samples passed through the sillimanite field during exhumation.

The lower LHS samples record a tight *P–T* loop as evidenced by sample 16. Despite significant garnet zoning in this sample (Fig. 2g), as the modal abundance of garnet is only ~2.5%, garnet growth probably caused limited fractionation of the bulk composition. The average garnet composition was therefore used to represent the composition of the peak assemblage of garnet, staurolite, biotite and ilmenite, stable at ~580 °C and ~8.5 kbar (Fig. 4).

### 4.3. U–Th–Pb monazite ages

Whereas the *P–T* data in this study indicate that the metamorphic history of samples from the same structural level across the MCT was similar, monazite ages yielded from the samples around the MCT exposure are different (Fig. 6; supplementary material S4 and supplementary data table).

Monazite ages in the structurally highest GHS samples range from ~37–14.5 Ma. 32 spots on 24 monazite grains in sample 343 yield ages ranging from: ~37–16 Ma (Fig. 7a): a matrix monazite core population yields an age of 26.2 ± 0.8 Ma (MSWD = 2.9, 11 analyses), monazites included in garnet yield an age of 22.7 ± 0.8 Ma (MSWD = 3, 7 analyses) and a matrix monazite rim population yields an age of 19.5 ± 0.4 Ma (MSWD = 1.7; 9 analyses; Fig. 7a). 21 spots on 11 monazites from sample 67 yield a spread in ages from ~37 to 14.6 Ma. A single monazite yields an age of ~37 Ma, monazite cores yield a rough age ~30 Ma, and 2–3 monazite rim analyses give a rough age of ~14.5 Ma (Fig. 6b, supplementary material S4.3.1). 30 spots on 18 monazite grains in sample 209 yield a younger, but overlapping spread in ages from ~17 Ma to 14.3 Ma (Fig. 6c, supplementary material S4.3.2).

The upper LHS samples (22, 30, 60) also yield a spread of ages ranging from ~21 to 12 Ma around the MCT exposure. 37 analyses from 14 monazite grains in sample 22 contained a spread in monazite ages from ~21 to 16 Ma. Y-poor cores yield an age of 20.8 ± 0.2 Ma (MSWD = 1.2; 12 analyses) and Y-rich rims yield an age of 15.6 ± 0.2 Ma (MSWD = 2.1; 4 analyses; Fig. 7b). 24 spots on 21 monazite grains in sample 60 yield evidence for several monazite populations, differentiated by textural inclusion relationships. 2 monazites included in garnet and staurolite cores yield spot ages of ~14.5 Ma. Monazites in garnet rims yield an age of 13.6 ± 0.1 Ma (MSWD = 1.7, 9 analyses). A population of monazites included within staurolite yield an age of 12.8 ± 0.2 Ma (MSWD = 1.7, 6 analyses). The youngest monazite population, comprising small unzoned matrix grains yield an age of 11.8 ± 0.2 Ma (MSWD = 1, 6 analyses; Fig. 6b; supplementary material S4.3.1). 14 analyses on 13 grains in sample 30 yield a limited dataset with difficult to interpret ages, ranging between ~24.5 and 11.5 Ma (Fig. 6c; supplementary material S4.3.2).

The samples from the lower LHS yield ages ranging from ~16 to 9 Ma. 22 analyses on 16 monazites in sample 16 yield a single population aged 15.9 ± 0.3 Ma (MSWD = 6.1; Fig. 7c). 24 analyses on 23 monazites in sample 97 yield ages ranging from ~10.5 to 9.3 Ma (Fig. 6b; supplementary material S4.3.1). 20 analyses on 18 monazites in sample 24 yield ages ranging from ~12.5 Ma to 10 Ma (Fig. 6c; supplementary material S4.3.2).

### 4.4. Monazite geochemistry

The monazite and garnet trace-element data for samples from the Takdah transect are summarised in Fig. 8 (the other transects are presented in the supplementary material S5 and in supplementary data table). The range in monazite and garnet trace-element concentrations does not systematically vary between GHS, upper and lower LHS samples. In general there is a trend where monazite cores are relatively more depleted in HREE-Y in comparison to the rims. Garnets show the opposite trend where the cores are generally more enriched in HREE-Y than the rims.

Specifically, monazite cores in GHS sample 343 are relatively depleted in HREE (average $Dy_N/Yb_N = 143$) and Y (~5500 ppm) in comparison to the rims (average $Dy_N/Yb_N = 30$; Y = ~15 000 ppm;

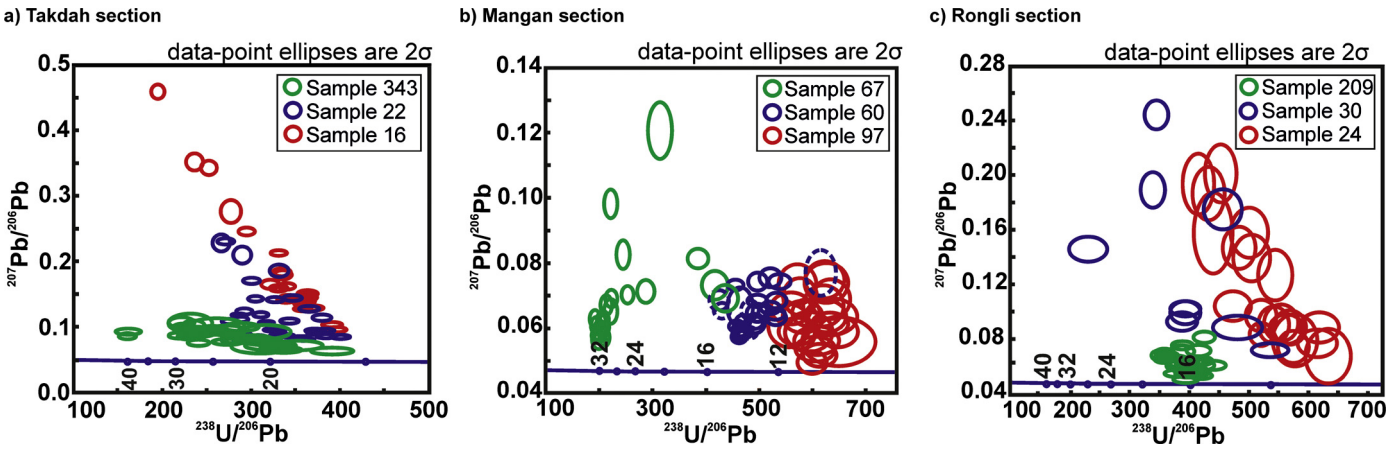


**Fig. 6.** Summary of all monazite U–Th–Pb data plotted in Tera–Wasserburg plots for the three sections from the Sikkim Himalaya (locations in Fig. 1). In each plot the structurally highest GHS sample is shown in green, the upper LHS sample in blue and the structurally lowest LHS sample in red. Detailed plots for each transect can be found in Fig. 7 for the Takdah transect, and in the supplementary material S4.3 for the Mangan and Rongli sections. (For interpretation of the references to colour in this figure legend, the reader is referred to the web version of this article.)

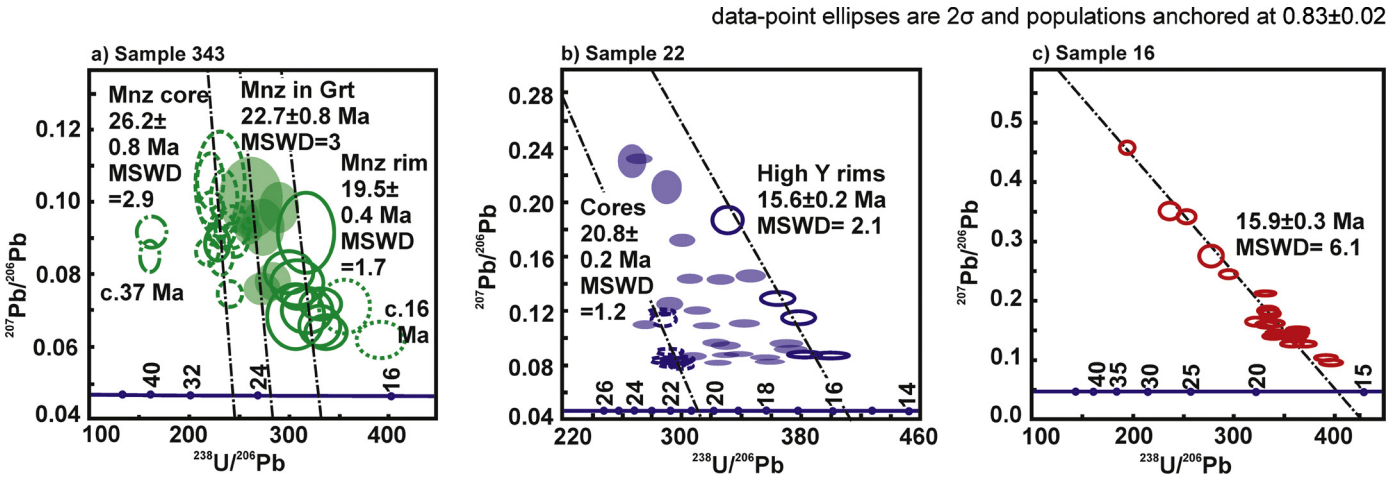


**Fig. 7.** Detailed Tera–Wasserburg plots for the Takdah transect. The GHS sample 343 in green, upper LHS sample 22 shown in blue and lower LHS sample 16 is shown in red. All data uncorrected for common Pb; intercepts are anchored at the common-Pb value of 0.83 ± 0.02 (Stacey and Kramers, 1975). (For interpretation of the references to colour in this figure legend, the reader is referred to the web version of this article.)

Fig. 2b), which display a pronounced Eu anomaly ($Eu/Eu^* = \sim 0.10–0.15$ in cores and ~0.2–0.3 in rims). Garnets show a fairly flat Y profile (400–900 ppm Y), with the rims showing a small depletion in HREE (average $Dy_N/Yb_N$ ratio = 1.4) in comparison with the cores (average $Dy_N/Yb_N$ ratio = 0.6; Fig. 8).

Monazite cores in upper LHS sample 22 are relatively depleted in HREE (average $Dy_N/Yb_N = 166$) and Y (<5000 ppm; Fig. 2d) in comparison with the more enriched rims ($Dy_N/Yb_N = 30$, Y = ~17 000 ppm). Garnet shows significant zoning in trace elements, in contrast to the flat profiles recorded for the major elements (Fig. 7d). The garnet cores are relatively enriched in Y and HREE and depleted in MREE (~600–900 ppm Y, $Dy_N/Yb_N = 1.2$) in comparison with the rims (~200–300 ppm Y, $Dy_N/Yb_N = 3.8$, Fig. 8).

Monazites in lower LHS sample 16 contain <6000 ppm Y (Fig. 2h), display a small Eu anomaly of ~0.5 and a $Dy_N/Yb_N$ ratio ranging from 16 to 171. Garnets show bell-shaped Y zoning and concentrations of up to ~2000 ppm.

## 5. Discussion

### 5.1. Linking monazite age to metamorphic stage

Monazite geochronology commonly yields complex datasets where a continuous spread of ages is seen (e.g. sample 22 in this study). In the past, these data types of dataset have been presented as probability density plots (e.g. Catlos et al., 2001; Corrie and Kohn, 2008; Rubatto et al., 2013), or have been interpreted as two end-member populations with analytical mixing in between (e.g. Dahl et al., 2005). Both interpretations provide limited insight into the causes of the yielded spread, and the interpretation of individual ages as documenting 'events' in geological time. The successful interpretation of metamorphic monazite ages requires the determination of the reactions which produced the monazite and the *P–T* conditions at which these reactions took place. Insight into both is provided by analysis of changes in diagnostic trace-element concentrations and ratios in monazite and co-crystallising major phases. The approach is outlined here for samples from the Takdah transect in detail; similar interpretations can be made for comparable samples from the other transects (supplementary material S5).

Overall the dataset suggests that the GHS rocks experienced a prolonged metamorphic history during which monazite grew as a product of several reactions. Monazite grains yield progressively younger ages, and record crystallisation over successively shorter timescales, at lower structural levels (Fig. 9).

GHS sample 343 yields monazites that grew over an extensive period of time, from ~37 to 16 Ma. The earliest reliable monazite population is represented by cores of matrix grains that yield

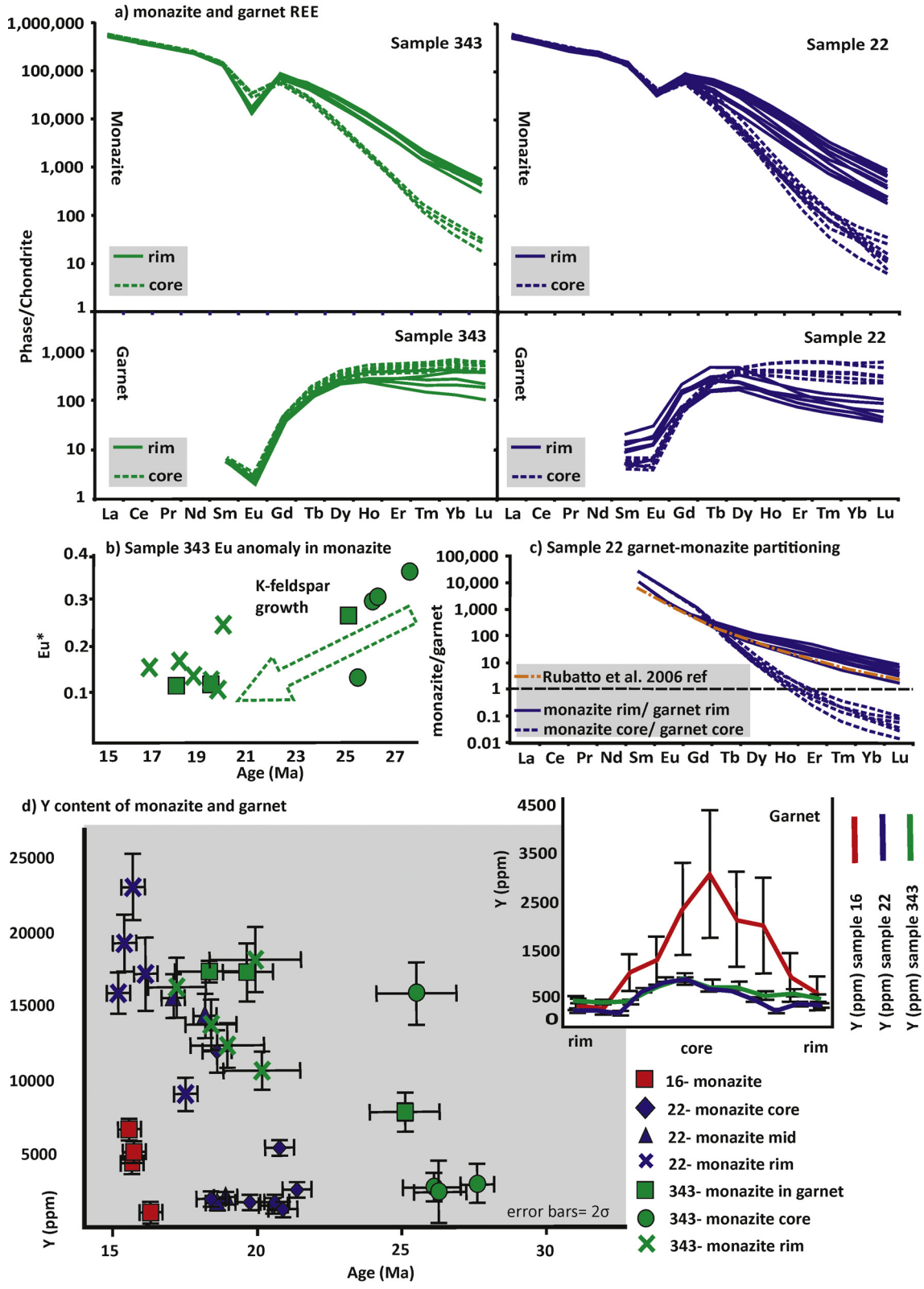


**Fig. 8.** Monazite and garnet geochemical data. (A) Monazite and garnet REE plots, normalised to chondritic values of McDonough and Sun (1995). In all plots core analyses are shown as dashed lines and rim analyses are shown as solid lines. Selected data for monazites and garnet from sample 343 is shown in green and sample 22 is shown in blue. (B) Plot showing the Eu anomaly (Eu*) plotted against the Th-corrected $^{206}Pb/^{238}U$ age for monazite in sample 343, with core analyses shown as circles and rims as crosses (same as for part d of figure). Lower Eu* values indicate K-feldspar growth as Eu is sequestered into feldspar during crystallisation. (C) Garnet–monazite partitioning for sample 22. The monazite REE data is normalised to the garnet REE data. Monazite rims are normalised to garnet rims and cores to cores. Reference data of Rubatto et al. (2006) are shown in orange. (D) Y content of monazites and garnet. Main plot shows Y against the Th-corrected $^{206}Pb/^{238}U$ age for monazite cores, rims and for grains included in garnets for samples 16 (red), 22 (blue) and 343 (green). Inset plot shows Y content across garnet profiles for samples 16, 22 and 343. (For interpretation of the references to colour in this figure legend, the reader is referred to the web version of this article.)

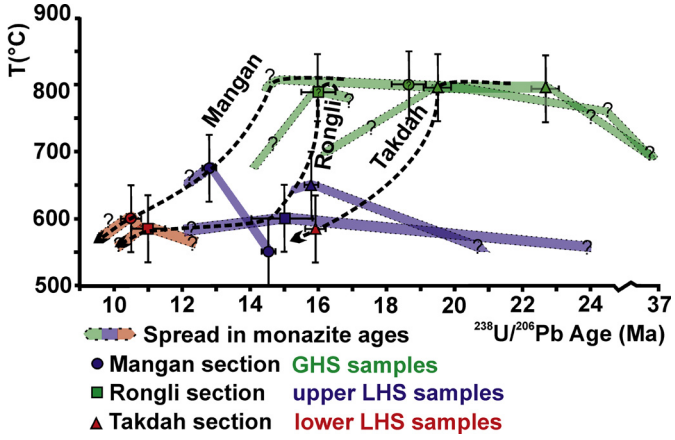


**Fig. 9.** Summary of the temperature and time ($T$–$t$) data for all samples presented in this study in the Takdah, Mangan and Rongli sections. The temperature (from pseudosection analysis, average temperature and Ti-in-biotite calculations, and which is tentatively linked to monazite ages as denoted by question marks) is plotted against the Th-corrected $^{206}Pb/^{238}U$ age for monazites at each point in the temperature history of each sample. Lower LHS sample histories are shown in red, upper LHS in blue, and GHS in green. Peak temperatures/monazite age are recorded by a symbol for each sample/section. The extended history of monazite growth for each sample is shown in the shaded elongate boxes. The dashed lines show the $T$–$t$ trajectory for each transect. (For interpretation of the references to colour in this figure legend, the reader is referred to the web version of this article.)

an age of 26.2 ± 0.8 Ma (MSWD = 2.9). These cores are depleted in HREE and Y and have a minor Eu anomaly (Fig. 8a). Monazites included in garnet and matrix monazite rims, however, yield younger ages of 22.7 ± 0.8 Ma (MSWD = 3) and 19.5 ± 0.4 Ma (MSWD = 1.7). Grains yielding these latter populations have a more pronounced Eu anomaly and show greater enrichment in HREE and Y (Fig. 8a, d). As Eu is preferentially incorporated into feldspars, particularly K-feldspar, during melt crystallisation (Buick et al., 2010; Fig. 8b), we interpret the monazite included in garnet (interpreted as a peritectic phase) and the rims of the matrix grains to constrain the time at which the rock experienced supra-solidus conditions (~790 °C and >10 kbar) to between ~23 and 19.5 Ma. Two further monazite analyses suggest continued monazite crystallisation until ~16 Ma.

Monazites in upper LHS sample 22 record ages from 20.8 ± 0.2 Ma (MSWD = 1.2) to 15.6 ± 0.2 Ma (MSWD = 2.1), indicating a prolonged metamorphic growth history. Allanite and xenotime inclusions in the HREE-enriched garnet cores indicate these phases were stable during prograde metamorphism. Their absence in the current matrix assemblage suggests they became unstable during garnet growth at higher grades (Fitzsimons et al., 2005; Janots et al., 2007; Smith and Barreiro, 1990). We therefore interpret the monazite cores, which are depleted in HREE, to have formed from the breakdown of allanite and xenotime at 20.8 ± 0.2 Ma (MSWD = 1.2), on the prograde path.

Monazite rims, in contrast, are enriched in HREE and Y. When normalised to garnet rim REE abundances, the monazite rims show trends that closely match experimental (supra-solidus) monazite-garnet partitioning data (Fig. 8c, Buick et al., 2006; Hermann and Rubatto, 2003; Rubatto et al., 2006). This suggests that the monazite rims grew in equilibrium with the garnet rims, and that the available HREE and Y were preferentially incorporated into monazite. Additionally, the close match between natural and experimental data suggests that equilibrium partitioning of HREE and Y between garnet and monazite is similar under both sub-solidus and supra-solidus conditions. The relationship between the HREE-Y concentrations in the two minerals may therefore be used to test for equilibrium.

Additional evidence for equilibrium between monazite rims and garnet rims comes from textural relationships. Monazite is included in garnet rims (grains were too small to analyse by laser ablation) and matrix grains are also found in close proximity to garnet. The matrix monazite rims yield an age of 15.6 ± 0.2 Ma (MSWD = 2.1). This age probably constrains the time of garnet rim growth during peak metamorphic conditions of ~650 °C and 8–10 kbar. Rutile inclusions in the garnet rim, yield Zr-in-rutile temperatures of 674.8 ± 9.4 °C, supporting the $P$–$T$ conditions determined from the pseudosection. The MREE enrichment in the garnet rim (Fig. 8a) suggests the breakdown of a MREE-enriched phase such as apatite or xenotime during garnet rim growth where the release of P may have assisted the growth of the monazite rims (Pyle and Spear, 2003; Simpson et al., 2000).

In many studies that document Himalayan monazite geochronology (e.g. Kohn et al., 2001; McQuarrie et al., 2014) the formation of high-Y monazite rims are linked to melt crystallisation or to garnet breakdown. Our data suggests that although high Y rims can be linked to melt crystallisation (for example matrix monazite rims in sample 343), high Y rims are also present in samples which equilibrated under subsolidus conditions. Furthermore, the garnet–monazite partitioning data suggests that the high Y monazite rims in sample 22 could have been growing in equilibrium with garnet rims, in association with the breakdown of another accessory phase such as apatite or xenotime, and therefore not during garnet breakdown. This demonstrates that although the assumption that high Y monazite forms during the breakdown of garnet may be valid for some samples, the trace-element budget of the rock is governed by complex relationships between the major and accessory phases, which can only be revealed by detailed use of petrochronology and petrological analysis.

Sample 16, collected from the lowest structural levels, contains allanite inclusions in garnet that indicate the former presence of allanite during prograde metamorphism (supplementary material S4.1). The breakdown reaction of allanite could have therefore been responsible for monazite formation at 15.9 ± 0.3 Ma (MSWD = 6.1) as metamorphic grade increased to ~580 °C and 8.5 kbar (Ferry, 2000; Janots et al., 2008; Krenn and Finger, 2007).

### 5.2. Metamorphic evolution of the MCT zone

The detailed petrochronological dataset presented here elucidates a specific and complex history of burial, thrusting and exhumation. Lowermost GHS samples 343 and 67 preserve evidence of an early (subsolidus) prograde history between ~37 and 26 Ma. Petrographic and trace-element chemistry evidence from sample 343 suggests that garnet and monazite crystallised coevally in the kyanite field and in the presence of melt between ~22.7 and 19.5 Ma. The rocks were then decompressed, and/or heated into the sillimanite field where samples 67 and 209 equilibrated (at ~17–14 Ma). Evidence of garnet/kyanite breakdown to hercynite in sample 72, adjacent to sample 67, suggests that the rocks decompressed into (and out of) the spinel field on the retrograde path.

At the same time the upper LHS rocks (initially in the footwall of the MCT) were buried and heated. This shows that although the GHS has an early history of deformation, temporally unrelated to the underlying footwall rocks, there is a later shared history of the two units. The early, prograde, monazite growth in all upper LHS samples overlaps with the final stages of monazite growth in the GHS samples; in the Takdah section, partial melting at peak conditions in the GHS coincided with prograde metamorphic conditions in the upper LHS samples at around 21–19.5 Ma. The upper LHS samples record protracted monazite growth over several million years. Monazite probably grew continuously: multiple resolvable populations of monazite are preserved within different index minerals in sample 60, demonstrating continuously evolving mineralogy from ~14.6 to 11.8 Ma at moderately high $P$–$T$ conditions (Fig. 9).

Monazite in the lower LHS samples began to grow during the last stages of monazite growth in the upper LHS samples (e.g. at 16 Ma in sample 16) and continued to crystallise until ~9 Ma in the northern-most samples.

This study therefore documents the diachronous attainment of peak metamorphic conditions through the inverted metamorphic sequence, with the timing, duration and grade of metamorphism decreasing with increasing structural depth through the thrust zone. Ages determined from samples from different exposures through the domed Sikkim MCT thrust zone also vary from north to south: spanning ~14.5–9 Ma in the northern (rear-ward) section and ~21–16 Ma in the southern (leading edge) section. Our dataset thus covers a >10 Ma 'time window' into the ductile thrusting history of the MCT.

Other studies have recorded monazite ages decreasing with depth below major thrust zones, both in the MCT zone, where monazite ages generally span between ~21 and 11 Ma throughout the central to eastern Himalaya (Bollinger and Janots, 2006; Catlos et al., 2004, 2001; Harrison et al., 1997; Kohn et al., 2001; Larson and Cottle, 2014; Larson et al., 2013; McQuarrie et al., 2014), and the Canadian Cordillera (Crowley and Parrish, 1999; Gibson et al., 1999). Monazite ages collected from this study are therefore in agreement with the age range yielded from previous studies. However recent analytical advances that allow higher precision data from smaller volumes of material and developments in understanding monazite petrochronology have provided new insight into the duration of ductile thrusting processes via different 'time windows' exposed in the Sikkim region.

Monazite grains yielding ages between 9 and 3 Ma reported from the MCT zone in the Nepal Himalaya (Bollinger and Janots, 2006; Harrison et al., 1997) have been cited as evidence for out-of-sequence thrusting along the MCT. In contrast to these previous studies, the comprehensive monazite dataset presented here implies that prolonged monazite growth was the product of several different reactions in multiple MCT transects, suggesting a model of continuous thrusting throughout the Miocene. The apparent lack of young (<9 Ma) monazites from the Sikkim Himalaya could be explained by differences in erosion horizon along the Himalaya, as demonstrated by the divergent ages from the leading and rear edge of the thrust zone presented in this study.

The $P$–$T$ evolution of samples from different structural levels presented in this study are also broadly in accord with previous estimates of the $P$–$T$ conditions from the MCT zone, both in Sikkim (Dasgupta et al., 2009, 2004; Dubey et al., 2005; Rubatto et al., 2013; Sorcar et al., 2014), and from similar structural levels elsewhere in the Himalaya (Caddick et al., 2007; Goscombe and Hand, 2000; Groppo et al., 2009; Kohn et al., 2001; Searle and Rex, 1989; Stephenson et al., 2000; Vannay and Grasemann, 1998; Yakymchuk and Godin, 2012). The constant pressures recorded throughout the thrust zone in the Sikkim Himalaya suggest that Indian crustal material was continuously buried to similar depths before exhumation. However the uncertainties on the pressure calculations, both in pseudosection and average $P$–$T$ analysis, make accurate interpretations difficult.

### 5.3. Model for inverted metamorphism development in the Sikkim Himalaya

The data from the Sikkim Himalaya point to a model where motion along the MCT caused successive burial and accretion of material from the footwall into the hanging wall. Accreted material was then transported southwards and upwards to progressively shallower levels (Fig. 10). This model is supported by evidence of tectonic interleaving of GHS and LHS protolith material in the Sikkim MCT zone (Mottram et al., 2014). We suggest that the thrust originally nucleated at the LHS–GHS protolith boundary. The plane of deformation migrated over time away from this 'parent thrust' down into its footwall over a period of ~5 Ma in each transect. The inverted metamorphic zone within the Sikkim Himalaya therefore records a series of 'paleothrusts', with each successive level representing a snapshot of MCT thrusting through time as material was accreted into the thrust zone. Accretion of material from the footwall into the hanging wall, decreasing peak metamorphic temperatures and progressively younger attainment of peak conditions are consequences of this model.

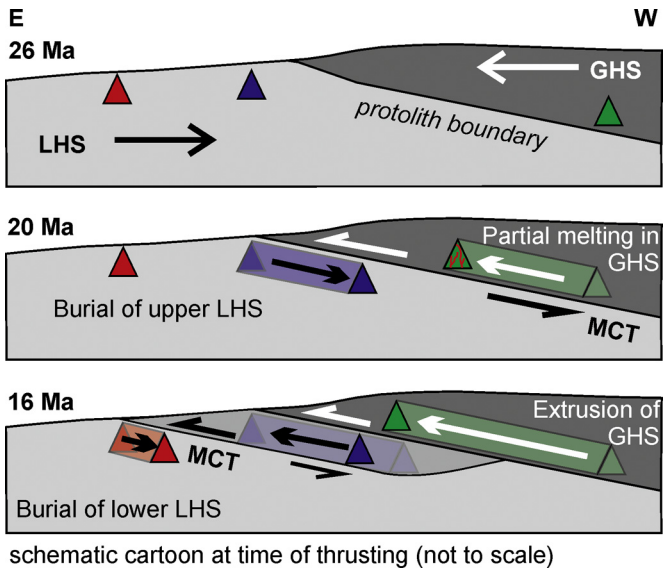


**Fig. 10.** Schematic cross section through the MCT (based on the Takdah section), showing the dynamic evolution of the thrust at three time periods; 26 Ma, 20 Ma and 16 Ma. At 26 Ma there was prograde metamorphism in the GHS which was separated from the LHS by a protolith boundary. At 20 Ma there was extrusion of the GHS accompanied by partial melting. The movement along the MCT led to burial of the upper LHS in the footwall of the thrust where prograde metamorphism occurred. At 16 Ma thrusting associated with the MCT penetrated down into what was once the footwall of the thrust. The upper LHS was extruded as part of the MCT hanging wall, burying the lower LHS in the footwall of the structure. At this time the lower LHS underwent rapid prograde metamorphism followed by extrusion by 16 Ma.

Our study provides petrochronological context to support previous models, based on more limited datasets, which are used to explain how material is accreted into thrust zones (e.g. Barr et al., 1986; Bollinger et al., 2004, 2006; Catlos et al., 2001; Harrison et al., 1998, 1997; Kohn et al., 2001). A similar accretion-mechanism to that found in the Sikkim Himalaya, is also predicted by both the channel flow and wedge-type Himalayan tectonic models (e.g. Beaumont et al., 2001; Jamieson et al., 2004; Kohn, 2008).

Heat sources for the development of inverted metamorphism have been widely discussed in the Himalayan literature (e.g. Burg et al., 1984; Duprat-Oualid et al., 2013; Harrison et al., 1998; Hubbard, 1996; Johnson and Strachan, 2006; Le Fort, 1975; Molnar and England, 1990; Pitra et al., 2010; Searle et al., 1999; Vannay and Grasemann, 2001). Although the dataset presented here from does not uniquely identify the heat sources for the inverted metamorphism, our data does provide some new insight into likely contributing sources.

It is firstly important to determine whether metamorphism and deformation were contemporaneous in the MCT zone. Our dataset includes ages from monazite inclusions within and associated with syn-kinematic metamorphic index minerals that are aligned and elongated along the main MCT sheared foliation (details in the supplementary material S2.3). This evidence suggests that metamorphism was intimately related, both texturally and temporally, to thrusting along the MCT.

Where hot rocks are thrust upon cold rocks (the hot iron model; Le Fort, 1975), the hanging wall is the heat source for metamorphism in the footwall. The data presented here clearly show that (decompressional) melting in the GHS hanging wall was contemporaneous with metamorphism in the upper LHS footwall, for at least the early period of thrusting. As anatexis is a consequence, rather than a cause, of heating and decompression (Harris et al., 1995), this suggests that the lower part of the GHS was at least hot enough to have melted and thus in bulk, could have provided the heat to drive the metamorphism of the footwall. In this way, heat was continuously advected to the footwall during progressive ductile thrusting. Accretion of footwall material to the hanging wall through time allowed the inverted metamorphic isotherms to be 'frozen' into the transect.

The data from the Sikkim Himalaya indicate that monazite continued to crystallise in the lower LHS footwall up to 5 Ma after the cessation of monazite crystallisation in the GHS hanging wall. It is important to note that although the hanging wall and footwall rocks are juxtaposed today, it is difficult to reconstruct their relative positions through the thrusting history (Jamieson et al., 1996). Despite this, it is possible that additional heat sources, other than a hot overriding GHS, are required in order to reproduce the temporal and thermal evolution of the LHS footwall rocks. It is therefore possible to suggest that heat advected from depth with the exhuming GHS was augmented by unusually high radiogenic heat flux generated from the K, U, Th-rich pelitic lithologies (England and Molnar, 1993; Inger and Harris, 1992; Johnson and Strachan, 2006; Ruppel and Hodges, 1994). Furthermore, the prolonged deformation and shearing that occurred during the down-cutting of the active thrust plane and the progressive accretion of the upper footwall to the hanging wall provides an additional possible heat source from shear heating (Arita, 1983; Bird, 1978; Duprat-Oualid et al., 2013; Kidder et al., 2013; Le Fort, 1975).

## 6. Conclusions

The MCT zone in the Sikkim Himalaya represents a zone of inverted metamorphism in which the age and grade of metamorphism decreases with depth within the thrust zone (by ~5 Ma and 250 °C respectively). Doming of the thrust after motion ceased permits unique insight into differences in timing of metamorphism along the transport direction. Our data show a 4–6 Ma difference in the timing of attainment of similar metamorphic conditions between the more northerly (rear-ward) and more southerly (leading edge) exposures through the structure. The highest structural levels of the MCT zone (lowermost GHS rocks) experienced peak metamorphic conditions of ~790 °C and 10 kbar at ~22.5–19.5 Ma in the southern exposure of the thrust zone and between ~30 and 20 Ma in the northern exposure. The upper LHS rocks reached peak metamorphic conditions of ~655 °C and 9 kbar at ~16 Ma in the south and ~12 Ma in the north. The lower LHS samples reached peak metamorphic conditions of ~580 °C and 8.5 kbar at ~16 Ma in the south, and between 10 and 9 Ma in the north. The inverted metamorphic zone within the Sikkim Himalaya therefore preserves a record of >10 Ma of the MCT thrusting history. During this time, material became progressively incorporated into the hanging wall from the footwall as the thrust zone continuously cut down-section, over a period of ~5 Ma. Thrusting is thought to have initiated from the original protolith boundary which represents the oldest active structure at the highest structural level of the thrust zone. Each slice of material that was incorporated into the thrust zone was metamorphosed during a consecutively younger metamorphic stage, by heating from the overthrust sheet, enhanced by radioactive heat production in the thrust zone and possibly by shear heating.

This study demonstrates the importance of combining spatially-resolved geochronology, trace-element geochemistry and $P$–$T$ modelling to link the monazite-forming reactions to the $P$–$T$ evolution recorded in the major rock-forming minerals. It is through such detailed petrochronology that we can fully interpret the temporal evolution of the rocks and demonstrate that inverted metamorphic sequences play an important role in preserving the duration of movement in progressively deforming ductile thrust zones.

## Acknowledgements

This study was funded by a UK Natural Environment Research Council (NERC) PhD studentship (NE/1528018/1) awarded to C.M.M and an NERC Advanced Fellowship (NE/H016279/1) awarded to C.J.W. Analytical work was funded by an NERC facility grant awarded to N.B.W.H (IP-1129-0511) and C.M.M for work at NERC Isotope Geosciences Laboratory (NIGL). We thank Michelle Higgins and Kay Green for help with sample preparation, Sam Hammond for technical support with ICP-MS, Andy Tindle for technical support with EPMA and Diane Johnson for help with the SEM. Mark Caddick is thanked for discussion about Perplex pseudosections. Saibal Gupta, Souvik Mitra, Lucy Greenwood, Tenpa Chophel and Kesang Sherpa are thanked for help in the field. Finally we acknowledge reviews from three anonymous reviewers that significantly improved the paper.

## Appendix A. Supplementary material

Supplementary material related to this article can be found online at http://dx.doi.org/10.1016/j.epsl.2014.07.006.

## References

Andreasson, P., Lagerblad, B., 1980. Occurrence and significance of inverted metamorphic gradients in the western Scandinavian Caledonides. J. Geol. Soc. 137, 219–230.

Arita, K., 1983. Origin of the inverted metamorphism of the Lower Himalayas, central Nepal. Tectonophysics 95, 43–60.

Baldwin, J., Powell, R., Williams, M., Goncalves, P., 2007. Formation of eclogite, and reaction during exhumation to mid-crustal levels, Snowbird tectonic zone, western Canadian Shield. J. Metamorph. Geol. 25, 953–974.

Barr, D., Holdsworth, R.E., Roberts, A.M., 1986. Caledonian ductile thrusting in a Precambrian metamorphic complex: the Moine of northwestern Scotland. Geol. Soc. Am. Bull. 97, 754–764.

Beaumont, C., Jamieson, R.A., Nguyen, M.H., Lee, B., 2001. Himalayan tectonics explained by extrusion of a low-viscosity crustal channel coupled to focused surface denudation. Nature 414, 738–742.

Bhattacharyya, K., Mitra, G., 2009. A new kinematic evolutionary model for the growth of a duplex – an example from the Rangit duplex, Sikkim Himalaya, India. Gondwana Res. 16, 697–715.

Bhattacharya, A., Mohanty, L., Maji, A., Sen, S., Raith, M., 1992. Non-ideal mixing in the phlogopite–annite binary: constraints from experimental data on Mg–Fe partitioning and a reformulation of the biotite–garnet geothermometer. Contrib. Mineral. Petrol. 111, 87–93.

Bird, P., 1978. Initiation of intracontinental subduction in the Himalaya. J. Geophys. Res., Solid Earth (1978–2012) 83, 4975–4987.

Bollinger, L., Avouac, J., Beyssac, O., Catlos, E., Harrison, T., Grove, M., Goffé, B., Sapkota, S., 2004. Thermal structure and exhumation history of the Lesser Himalaya in central Nepal. Tectonics 23, TC5015.

Bollinger, L., Henry, P., Avouac, J., 2006. Mountain building in the Nepal Himalaya: thermal and kinematic model. Earth Planet. Sci. Lett. 244, 58–71.

Bollinger, L., Janots, E., 2006. Evidence for Mio-Pliocene retrograde monazite in the Lesser Himalaya, far western Nepal. Eur. J. Mineral. 18, 289–297.

Buick, I., Clark, C., Rubatto, D., Hermann, J., Pandit, M., Hand, M., 2010. Constraints on the Proterozoic evolution of the Aravalli–Delhi Orogenic belt (NW India) from monazite geochronology and mineral trace element geochemistry. Lithos 120, 511–528.

Buick, I.S., Hermann, J., Williams, I.S., Gibson, R.L., Rubatto, D., 2006. A SHRIMP U–Pb and LA-ICP-MS trace element study of the petrogenesis of garnet–cordierite–orthoamphibole gneisses from the Central Zone of the Limpopo Belt, South Africa. Lithos 88, 150–172.

Burg, J., Matte, P., Leyreloup, A., Marchand, J., 1984. Inverted metamorphic zonation and large-scale thrusting in the Variscan Belt: an example in the French Massif Central. Geol. Soc. (Lond.) Spec. Publ. 14, 47–61.
Caddick, M., Bickle, M., Harris, N., Holland, T., Horstwood, M., Parrish, R.R., Ahmad, T., 2007. Burial and exhumation history of a Lesser Himalayan schist: recording the formation of an inverted metamorphic sequence in NW India. Earth Planet. Sci. Lett. 264, 375–390.
Camiré, G., La Fleche, M., Jenner, G., 1995. Geochemistry of pre-Taconian mafic volcanism in the Humber Zone of the northern Appalachians, Québec, Canada. Chem. Geol. 119, 55–77.
Catlos, E.J., Dubey, C.S., Harrison, T.M., Edwards, M.A., 2004. Late Miocene movement within the Himalayan Main Central Thrust shear zone, Sikkim, north–east India. J. Metamorph. Geol. 22, 207–226.
Catlos, E.J., Harrison, T.M., Kohn, M.J., Grove, M., Ryerson, F.J., Manning, C.E., Upreti, B.N., 2001. Geochronologic and thermobarometric constraints on the evolution of the Main Central Thrust, central Nepal Himalaya. J. Geophys. Res., Solid Earth 106, 16177–16204.
Connolly, J., 1990. Multivariable phase diagrams; an algorithm based on generalized thermodynamics. Am. J. Sci. 290, 666–718.
Connolly, J., 2009. The geodynamic equation of state: what and how. Geochem. Geophys. Geosyst. 10.
Corrie, S.L., Kohn, M.J., 2008. Trace-element distributions in silicates during prograde metamorphic reactions: implications for monazite formation. J. Metamorph. Geol. 26, 451–464.
Crowley, J., Parrish, R., 1999. U–Pb isotopic constraints on diachronous metamorphism in the northern Monashee complex, southern Canadian Cordillera. J. Metamorph. Geol. 17, 483–502.
Dahl, P.S., Hamilton, M.A., Jercinovic, M.J., Terry, M.P., Williams, M.L., Frei, R., 2005. Comparative isotopic and chemical geochronometry of monazite, with implications for U–Th–Pb dating by electron microprobe: an example from metamorphic rocks of the eastern Wyoming Craton (USA). Am. Mineral. 90, 619–638.
Dasgupta, S., Chakraborty, S., Neogi, S., 2009. Petrology of an inverted Barrovian Sequence of metapelites in Sikkim Himalaya, India: constraints on the tectonics of inversion. Am. J. Sci. 309, 43–84.
Dasgupta, S., Ganguly, J., Neogi, S., 2004. Inverted metamorphic sequence in the Sikkim Himalayas: crystallization history, $P$–$T$ gradient and implications. J. Metamorph. Geol. 22, 395–412.
Dubey, C.S., Catlos, E.J., Sharma, B.K., 2005. Modelling of $P$–$T$–$t$ paths constrained by mineral chemistry and monazite dating of metapelites in relationship to MCT activity in Sikkim Eastern Himalayas. In: Thomas, H. (Ed.), Metamorphism and Crustal Evolution. Atlantic Publishers, New Delhi, pp. 250–282.
Duprat-Oualid, S., Yamato, P., Pitra, P., 2013. Major role of shear heating in intracontinental inverted metamorphism: inference from a thermo-kinematic parametric study. Tectonophysics.
England, P., Molnar, P., 1993. The interpretation of inverted metamorphic isograds using simple physical calculations. Tectonics 12, 145–157.
Evans, T., 2004. A method for calculating effective bulk composition modification due to crystal fractionation in garnet-bearing schist: implications for isopleth thermobarometry. J. Metamorph. Geol. 22, 547–557.
Ferry, J.M., 2000. Patterns of mineral occurrence in metamorphic rocks. Am. Mineral. 85, 1573–1588.
Fitzsimons, I., Kinny, P., Wetherley, S., Hollingsworth, D., 2005. Bulk chemical control on metamorphic monazite growth in pelitic schists and implications for U–Pb age data. J. Metamorph. Geol. 23, 261–277.
Foster, G., Gibson, H., Parrish, R., Horstwood, M., Fraser, J., Tindle, A., 2002. Textural, chemical and isotopic insights into the nature and behaviour of metamorphic monazite. Chem. Geol. 191, 183–207.
Foster, G., Kinny, P., Vance, D., Prince, C., Harris, N., 2000. The significance of monazite U–Th–Pb age data in metamorphic assemblages; a combined study of monazite and garnet chronometry. Earth Planet. Sci. Lett. 181, 327–340.
Foster, G., Parrish, R.R., Horstwood, M.S., Chenery, S., Pyle, J., Gibson, H., 2004. The generation of prograde $P$–$T$–$t$ points and paths; a textural, compositional, and chronological study of metamorphic monazite. Earth Planet. Sci. Lett. 228, 125–142.
Gaidies, F., Abart, R., De Capitani, C., Schuster, R., Connolly, J., Reusser, E., 2006. Characterization of polymetamorphism in the Austroalpine basement east of the Tauern Window using garnet isopleth thermobarometry. J. Metamorph. Geol. 24, 451–475.
Gansser, A., 1964. Geology of the Himalayas. Interscience, London, 289 pp.
Gasser, D., Bruand, E., Rubatto, D., Stüwe, K., 2012. The behaviour of monazite from greenschist facies phyllites to anatectic gneisses: an example from the Chugach Metamorphic Complex, southern Alaska. Lithos 134, 108–122.
Gibson, H.D., Brown, R.L., Parrish, R.R., 1999. Deformation-induced inverted metamorphic field gradients: an example from the southeastern Canadian Cordillera. J. Struct. Geol. 21, 751–767.
Goscombe, B., Hand, M., 2000. Contrasting $P$–$T$ paths in the Eastern Himalaya, Nepal: inverted isograds in a paired metamorphic mountain belt. J. Petrol. 41, 1673–1719.
Groppo, C., Rolfo, F., Lombardo, B., 2009. $P$–$T$ evolution across the Main Central Thrust Zone (Eastern Nepal): hidden discontinuities revealed by petrology. J. Petrol. 50, 1149–1180.
Groppo, C., Rubatto, D., Rolfo, F., Lombardo, B., 2010. Early oligocene partial melting in the main central thrust zone (Arun valley, eastern Nepal Himalaya). Lithos 118, 287–301.
Harris, N., Ayres, M., Massey, J., 1995. Geochemistry of granitic melts produced during the incongruent melting of muscovite: implications for the extraction of Himalayan leucogranite magmas. J. Geophys. Res., Solid Earth (1978–2012) 100, 15767–15777.
Harrison, T.M., Grove, M., Lovera, O.M., Catlos, E., 1998. A model for the origin of Himalayan anatexis and inverted metamorphism. J. Geophys. Res., Solid Earth (1978–2012) 103, 27017–27032.
Harrison, T.M., Ryerson, F.J., LeFort, P., Yin, A., Lovera, O.M., Catlos, E.J., 1997. A Late Miocene–Pliocene origin for the Central Himalayan inverted metamorphism. Earth Planet. Sci. Lett. 146, E1–E7.
Henry, D.J., Guidotti, C.V., Thomson, J.A., 2005. The Ti-saturation surface for low-to-medium pressure metapelitic biotites: implications for geothermometry and Ti-substitution mechanisms. Am. Mineral. 90, 316–328.
Hermann, J., Rubatto, D., 2003. Relating zircon and monazite domains to garnet growth zones: age and duration of granulite facies metamorphism in the Val Malenco lower crust. J. Metamorph. Geol. 21, 833–852.
Hoisch, T.D., Wells, M.L., Grove, M., 2008. Age trends in garnet-hosted monazite inclusions from upper amphibolite facies schist in the northern Grouse Creek Mountains, Utah. Geochim. Cosmochim. Acta 72, 5505–5520.
Holland, T., Powell, R., 2011. An improved and extended internally consistent thermodynamic dataset for phases of petrological interest, involving a new equation of state for solids. J. Metamorph. Geol. 29, 333–383.
Hubbard, M., 1996. Ductile shear as a cause of inverted metamorphism: example from the Nepal Himalaya. J. Geol. 493–499.
Inger, S., Harris, N., 1992. Tectonothermal evolution of the High Himalayan crystalline sequence, Langtang Valley, northern Nepal. J. Metamorph. Geol. 10, 439–452.
Jamieson, R., 1986. $P$–$T$ paths from high temperature shear zones beneath ophiolites. J. Metamorph. Geol. 4, 3–22.
Jamieson, R., Beaumont, C., Hamilton, J., Fullsack, P., 1996. Tectonic assembly of inverted metamorphic sequences. Geology 24, 839–842.
Jamieson, R.A., Beaumont, C., Medvedev, S., Nguyen, M.H., 2004. Crustal channel flows: 2. Numerical models with implications for metamorphism in the Himalayan–Tibetan orogen. J. Geophys. Res. 109, B06407.
Janots, E., Brunet, F., Goffé, B., Poinssot, C., Burchard, M., Cemič, L., 2007. Thermochemistry of monazite-(La) and dissakisite-(La): implications for monazite and allanite stability in metapelites. Contrib. Mineral. Petrol. 154, 1–14.
Janots, E., Engi, M., Berger, A., Allaz, J., Schwarz, J.O., Spandler, C., 2008. Prograde metamorphic sequence of REE minerals in pelitic rocks of the Central Alps: implications for allanite–monazite–xenotime phase relations from 250 to 610 °C. J. Metamorph. Geol. 26, 509–526.
Janots, E., Engi, M., Rubatto, D., Berger, A., Gregory, C., Rahn, M., 2009. Metamorphic rates in collisional orogeny from in situ allanite and monazite dating. Geology 37, 11–14.
Janots, E., Negro, F., Brunet, F., Goffé, B., Engi, M., Bouybaouène, M.L., 2006. Evolution of the REE mineralogy in HP–LT metapelites of the Sebtide complex, Rif, Morocco: monazite stability and geochronology. Lithos 87, 214–234.
Johnson, M., Strachan, R., 2006. A discussion of possible heat sources during nappe stacking: the origin of Barrovian metamorphism within the Caledonian thrust sheets of NW Scotland. J. Geol. Soc. 163, 579–582.
Kidder, S.B., Herman, F., Saleeby, J., Avouac, J.-P., Ducea, M.N., Chapman, A., 2013. Shear heating not a cause of inverted metamorphism. Geology 41, 1007–1010.
Kingsbury, J.A., Miller, C.F., Wooden, J.L., Harrison, T.M., 1993. Monazite paragenesis and U–Pb systematics in rocks of the eastern Mojave Desert, California, USA: implications for thermochronometry. Chem. Geol. 110, 147–167.
Kohn, M.J., 2008. $P$–$T$–$t$ data from central Nepal support critical taper and repudiate large-scale channel flow of the Greater Himalayan Sequence. Geol. Soc. Am. Bull. 120, 259–273.
Kohn, M.J., Catlos, E.J., Ryerson, F.J., Harrison, T.M., 2001. Pressure–temperature–time path discontinuity in the Main Central thrust zone, central Nepal. Geology 29, 571–574.
Krenn, E., Finger, F., 2007. Formation of monazite and rhabdophane at the expense of allanite during Alpine low temperature retrogression of metapelitic basement rocks from Crete, Greece: microprobe data and geochronological implications. Lithos 95, 130–147.
Larson, K.P., Cottle, J.M., 2014. Midcrustal Discontinuities and the Assembly of the Himalayan mid-crust. Tectonics 33, 718–740.
Larson, K.P., Gervais, F., Kellett, D.A., 2013. A $P$–$T$–$t$–$D$ discontinuity in east–central Nepal: implications for the evolution of the Himalayan mid-crust. Lithos 179, 275–292.
Le Fort, P., 1975. Himalayas: the collided range. Present knowledge of the continental arc. Am. J. Sci. 275 A, 1–44.
Ludwig, K.R., 2003. A geochronological toolkit for microsoft excel. Berkeley Geochronology Center. Special Publication no. 4, 71 pp.
McDonough, W.F., Sun, S.-S., 1995. The composition of the Earth. Chem. Geol. 120, 223–253.

McQuarrie, N., Tobgay, T., Long, S.P., Reiners, P.W., Cosca, M.A., 2014. Variable exhumation rates and variable displacement rates: documenting recent slowing of Himalayan shortening in western Bhutan. Earth Planet. Sci. Lett. 386, 161–174.
Mohan, A., Windley, B.F., Searle, M.P., 1989. Geothermobarometry and development of inverted metamorphism in the Darjeeling Sikkim region of the eastern Himalaya. J. Metamorph. Geol. 7, 95–110.
Molnar, P., England, P., 1990. Temperatures, heat flux, and frictional stress near major thrust faults. J. Geophys. Res., Solid Earth (1978–2012) 95, 4833–4856.
Mottram, C.M., Argles, T., Parrish, R., Harris, N., Horstwood, M., Gupta, S., 2014. Tectonic interleaving along the Main Central Thrust, Sikkim Himalaya. J. Geol. Soc. 171, 255–268.
Palin, R., Searle, M., Waters, D., Parrish, R., Roberts, N., Horstwood, M., Yeh, M.W., Chung, S.L., Anh, T., 2013. A geochronological and petrological study of anatectic paragneiss and associated granite dykes from the Day Nui Con Voi metamorphic core complex, North Vietnam: constraints on the timing of metamorphism within the Red River shear zone. J. Metamorph. Geol. 31, 359–387.
Parrish, R.R., 1990. U–Pb dating of monazite and its application to geological problems. Can. J. Earth Sci. 27, 1431–1450.
Paudel, L.P., Arita, K., 2000. Tectonic and polymetamorphic history of the Lesser Himalaya in central Nepal. J. Asian Earth Sci. 18, 561–584.
Pitra, P., Ballevre, M., Ruffet, G., 2010. Inverted metamorphic field gradient towards a Variscan suture zone (Champtoceaux Complex, Armorican Massif, France). J. Metamorph. Geol. 28, 183–208.
Powell, R., Holland, T.J.B., 1988. An internally consistent dataset with uncertainties and correlations. 3. Applications to geobarometry, worked examples and a computer program. J. Metamorph. Geol. 6, 173–204.
Pyle, J.M., Spear, F.S., 2003. Four generations of accessory-phase growth in low-pressure migmatites from SW New Hampshire. Am. Mineral. 88, 338–351.
Rubatto, D., Chakraborty, S., Dasgupta, S., 2013. Timescales of crustal melting in the Higher Himalayan Crystallines (Sikkim, Eastern Himalaya) inferred from trace element-constrained monazite and zircon chronology. Contrib. Mineral. Petrol. 165, 349–372.
Rubatto, D., Hermann, J., Buick, I.S., 2006. Temperature and bulk composition control on the growth of monazite and zircon during low-pressure anatexis (Mount Stafford, central Australia). J. Petrol. 47, 1973–1996.
Ruppel, C., Hodges, K., 1994. Pressure–temperature–time paths from two-dimensional thermal models: prograde, retrograde, and inverted metamorphism. Tectonics 13, 17–44.
Schneider, C.A., Rasband, W.S., Eliceiri, K.W., 2012. NIH Image to ImageJ: 25 years of image analysis. Nat. Methods 9, 671–675.
Searle, M., Waters, D., Dransfield, M., Stephenson, B., Walker, C., Walker, J., Rex, D., 1999. Thermal and mechanical models for the structural and metamorphic evolution of the Zanskar High Himalaya. Geol. Soc. (Lond.) Spec. Publ. 164, 139–156.
Searle, M.P., Rex, A., 1989. Thermal model for the Zanskar Himalaya. J. Metamorph. Geol. 7, 127–134.
Simpson, R.L., Parrish, R.R., Searle, M.P., Waters, D.J., 2000. Two episodes of monazite crystallization during metamorphism and crustal melting in the Everest region of the Nepalese Himalaya. Geology 28, 403–406.
Sinha-Roy, S., 1982. Himalayan Main Central Thrust and its implications for Himalayan inverted metamorphism. Tectonophysics 84, 197–224.
Smith, H.A., Barreiro, B., 1990. Monazite U–Pb dating of staurolite grade metamorphism in pelitic schists. Contrib. Mineral. Petrol. 105, 602–615.
Sorcar, N., Hoppe, U., Dasgupta, S., Chakraborty, S., 2014. High-temperature cooling histories of migmatites from the High Himalayan Crystallines in Sikkim, India: rapid cooling unrelated to exhumation? Contrib. Mineral. Petrol. 167, 1–34.
Spear, F.S., 2010. Monazite–allanite phase relations in metapelites. Chem. Geol. 279, 55–62.
Stacey, J.S., Kramers, J.P., 1975. Approximation of terrestrial lead isotope evolution by a two-stage model. Earth Planet. Sci. Lett. 26, 207–221.
Stephenson, B.J., Waters, D.J., Searle, M.P., 2000. Inverted metamorphism and the main central thrust: field relations and thermobarometric constraints from the Kishtwar Window, NW Indian Himalaya. J. Metamorph. Geol. 18, 571–590.
Tomkins, H., Powell, R., Ellis, D., 2007. The pressure dependence of the zirconium-in-rutile thermometer. J. Metamorph. Geol. 25, 703–713.
Vannay, J.-C., Grasemann, B., 2001. Himalayan inverted metamorphism and synconvergence extension as a consequence of a general shear extrusion. Geol. Mag. 138, 253–276.
Vannay, J., Grasemann, B., 1998. Himalayan inverted metamorphism in the High Himalaya of Kinnaur (NW India): petrography versus thermobarometry. Schweiz. Mineral. Petrogr. Mitt. 78, 107–132.
Vannay, J.-C., Sharp, Z.D., Grasemann, B., 1999. Himalayan inverted metamorphism constrained by oxygen isotope thermometry. Contrib. Mineral. Petrol. 137, 90–101.
Waters, D.J., 2001. The significance of prograde and retrograde quartz-bearing intergrowth microstructures in partially melted granulite-facies rocks. Lithos 56, 97–110.
White, R.W., Powell, R., Holland, T.J.B., 2007. Progress relating to calculation of partial melting equilibria for metapelites. J. Metamorph. Geol. 25, 511–527.
Wing, B.A., Ferry, J.M., Harrison, T.M., 2003. Prograde destruction and formation of monazite and allanite during contact and regional metamorphism of pelites: petrology and geochronology. Contrib. Mineral. Petrol. 145, 228–250.
Yakymchuk, C., Godin, L., 2012. Coupled role of deformation and metamorphism in the construction of inverted metamorphic sequences: an example from far-northwest Nepal. J. Metamorph. Geol. 30, 513–535.